

# Planck pre-launch status: Low Frequency Instrument calibration and expected scientific performance

A. Mennella<sup>1</sup>, M. Bersanelli<sup>1</sup>, R. C. Butler<sup>2</sup>, F. Cuttaia<sup>2</sup>, O. D’Arcangelo<sup>3</sup>, R. J. Davis<sup>4</sup>, M. Frailis<sup>5</sup>, S. Galeotta<sup>5</sup>, A. Gregorio<sup>6</sup>, C. R. Lawrence<sup>7</sup>, R. Leonardi<sup>8</sup>, S. R. Lowe<sup>4</sup>, N. Mandolesi<sup>2</sup>, M. Maris<sup>5</sup>, P. Meinhold<sup>8</sup>, L. Mendes<sup>9</sup>, G. Morgante<sup>2</sup>, M. Sandri<sup>2</sup>, L. Stringhetti<sup>2</sup>, L. Terenzi<sup>2</sup>, M. Tomasi<sup>1</sup>, L. Valenziano<sup>2</sup>, F. Villa<sup>2</sup>, A. Zacchei<sup>5</sup>, A. Zonca<sup>10</sup>, M. Balasini<sup>11</sup>, C. Franceschet<sup>1</sup>, P. Battaglia<sup>11</sup>, P. M. Lapolla<sup>11</sup>, P. Leutenegger<sup>11</sup>, M. Miccolis<sup>11</sup>, L. Pagan<sup>11</sup>, R. Silvestri<sup>11</sup>, B. Aja<sup>12</sup>, E. Artal<sup>12</sup>, G. Baldan<sup>11</sup>, P. Bastia<sup>11</sup>, T. Bernardino<sup>13</sup>, L. Boschini<sup>11</sup>, G. Cafagna<sup>11</sup>, B. Cappellini<sup>10</sup>, F. Cavaliere<sup>1</sup>, F. Colombo<sup>11</sup>, L. de La Fuente<sup>12</sup>, J. Edgeley<sup>4</sup>, M. C. Falvella<sup>14</sup>, F. Ferrari<sup>11</sup>, S. Fogliani<sup>5</sup>, E. Franceschi<sup>2</sup>, T. Gaier<sup>7</sup>, F. Gomez<sup>15</sup>, J. M. Herreros<sup>15</sup>, S. Hildebrandt<sup>15</sup>, R. Hoyland<sup>15</sup>, N. Hughes<sup>16</sup>, P. Jukkala<sup>16</sup>, D. Kettle<sup>4</sup>, M. Laaninen<sup>17</sup>, D. Lawson<sup>4</sup>, P. Leahy<sup>4</sup>, S. Levin<sup>15</sup>, P. B. Lilje<sup>18</sup>, D. Maino<sup>1</sup>, M. Malaspina<sup>2</sup>, P. Manzato<sup>5</sup>, J. Marti-Canales<sup>19</sup>, E. Martinez-Gonzalez<sup>13</sup>, A. Mediavilla<sup>12</sup>, F. Pasian<sup>5</sup>, J. P. Pascual<sup>12</sup>, M. Pecora<sup>11</sup>, L. Peres-Cuevas<sup>20</sup>, P. Platania<sup>3</sup>, M. Pospieszalsky<sup>21</sup>, T. Poutanen<sup>22,23,24</sup>, R. Rebolo<sup>16</sup>, N. Roddis<sup>4</sup>, M. Salmon<sup>13</sup>, M. Seiffert<sup>7</sup>, A. Simonetto<sup>3</sup>, C. Sozzi<sup>3</sup>, J. Tauber<sup>20</sup>, J. Tuovinen<sup>25</sup>, J. Varis<sup>25</sup>, A. Wilkinson<sup>4</sup>, and F. Winder<sup>4</sup>

(Affiliations can be found after the references)

## ABSTRACT

We give the calibration and scientific performance parameters of the Planck Low Frequency Instrument (LFI) measured during the ground cryogenic test campaign. These parameters characterise the instrument response and constitute our best pre-launch knowledge of the LFI scientific performance. The LFI shows excellent  $1/f$  stability and rejection of instrumental systematic effects; measured noise performance shows that LFI is the most sensitive instrument of its kind. The set of measured calibration parameters will be updated during flight operations through the end of the mission.

**Key words.** Cosmic Microwave Background, Cosmology, Space Instrumentation, Coherent Receivers, Calibration and Testing

## 1. Introduction

The Low Frequency Instrument (LFI) is an array of 22 coherent differential receivers at 30, 44, and 70 GHz on board the European Space Agency Planck<sup>1</sup> satellite. In 15 months<sup>2</sup> of continuous measurements from the Lagrangian point  $L_2$  Planck will provide cosmic-variance- and foreground-limited measurements of the Cosmic Microwave Background temperature anisotropies by scanning the sky in near great circles with a 1.5 m dual reflector aplanatic telescope (Tauber 2009; Martin et al. 2004; Villa et al. 2002; Dupac & Tauber 2005).

The LFI shares the focal plane of the Planck telescope with the High Frequency Instrument (HFI), an array of 52 bolometers in the 100–857 GHz range, cooled to 0.1 K. This wide frequency coverage, required for optimal component separation, constitutes a unique feature of Planck and a formidable technological challenge, with the integra-

tion of two different technologies with different cryogenic requirements in the same focal plane.

Excellent noise performance is obtained with receivers based on indium phosphide high electron mobility transistor amplifiers, cryogenically cooled to 20 K by a vibrationless hydrogen sorption cooler, which provides more than 1 W of cooling power at 20 K. The LFI thermal design has been driven by an optimisation of receiver sensitivity and available cooling power; in particular radio frequency (RF) amplification is divided between a 20 K front-end unit and a  $\sim 300$  K back-end unit connected by composite waveguides (Bersanelli et al. 2009).

The LFI has been developed following a modular approach in which the various sub-units (passive components, receiver active components, electronics, etc.) have been built and tested individually before proceeding to the next integration step. The final integration and testing phases have been the assembly, verification, and calibration of the individual radiometer chains (Villa et al. 2009) and of the integrated instrument.

In this paper we focus on calibration, i.e., the set of parameters that provides our current best knowledge of the instrument’s scientific performance. After an overview of the calibration philosophy we focus on the main calibration parameters measured during test campaigns performed at instrument and satellite levels. Information concerning the test setup and data analysis methods is provided where

Send offprint requests to: Aniello Mennella

<sup>1</sup> Planck (<http://www.esa.int/Planck>) is a project of the European Space Agency - ESA - with instruments provided by two scientific Consortia funded by ESA member states (in particular the lead countries: France and Italy) with contributions from NASA (USA), and telescope reflectors provided in a collaboration between ESA and a scientific Consortium led and funded by Denmark.

<sup>2</sup> There are enough consumables on board to allow operation for an additional year.

necessary, with references to appropriate technical articles for further details. The companion article that describes the LFI instrument (Bersanelli et al. 2009) is the most central reference for this paper.

The naming convention that we use for receivers and individual channels is given in Appendix A.

## 2. Overview of the LFI pseudo correlation architecture

In this section we briefly summarise the LFI pseudo-correlation architecture. Further details and a more complete treatment of the instrument can be found in Bersanelli et al. (2009).

In the LFI each receiver couples with the Planck telescope secondary mirror via a corrugated feed horn feeding an orthomode transducer (OMT) that splits the incoming wave into two perpendicularly polarised components, which propagate through two independent pseudo correlation receivers with HEMT (High Electron Mobility Transistor) amplifiers split between a cold ( $\sim 20$  K) and a warm ( $\sim 300$  K) stage connected by composite waveguides.

A schematic of the LFI pseudo correlation receiver is shown in Fig. 1. In each radiometer connected to an OMT arm, the sky signal and the signal from a stable reference load thermally connected to the HFI 4 K shield (Valenziano et al. 2009) are coupled to cryogenic low-noise HEMT amplifiers via a  $180^\circ$  hybrid. One of the two signals runs through a switch that applies a phase shift which oscillates between 0 and  $180^\circ$  at a frequency of 4096 Hz. A second phase switch is present for symmetry on the second radiometer leg but it does not introduce any phase shift. The signals are then recombined by a second  $180^\circ$  hybrid coupler, producing a sequence of sky-load outputs alternating at twice the frequency of the phase switch.

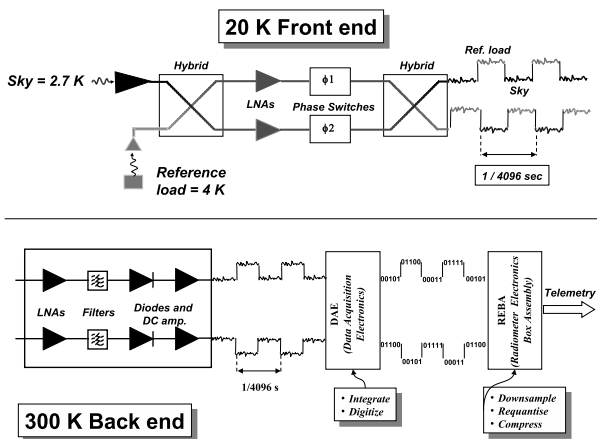


**Fig. 1.** Schematic of the LFI pseudo correlation architecture

In the back-end of each radiometer (see bottom part of Fig. 1) the RF signals are further amplified, filtered by a low-pass filter and then detected. After detection the sky and reference load signals are integrated and digitised in 14-bit integers by the LFI DAE (Digital Acquisition Electronics) box.

According to the scheme described above the radiometric differential power output from each diode can be written as:

$$p_{\text{out}} = aG_{\text{tot}}k\beta [T_{\text{sky}} + T_{\text{noise}} - r(T_{\text{ref}} + T_{\text{noise}})]$$

$$r = \frac{\langle V_{\text{out}}^{\text{sky}} \rangle}{\langle V_{\text{out}}^{\text{ref}} \rangle} \quad (1)$$

where the gain modulation factor,  $r$ , minimises the effect of the input signal offset between the sky ( $\sim 2.7$  K) and the reference load ( $\sim 4.5$  K). The effect of reducing the offset in software and the way  $r$  is estimated from flight data are discussed in detail in Mennella et al. (2003).

## 3. Calibration philosophy

The LFI calibration plan was designed to ensure optimal measurement of all parameters characterising the instrument response. Calibration activities have been performed at various levels of integration, from single components, to the integrated instrument, to the whole satellite. The inherent redundancy of this approach provided maximum knowledge of the instrument and of its sub-units, as well as calibration at different levels.

Table 1 gives the main LFI instrument parameters and the integration levels at which they have been measured. Three main groups of calibration activities are identified: (i) basic calibration (Sect. 5.1), (ii) receiver noise properties (Sect. 5.2), and (iii) susceptibility (Sect. 5.3).

A particular point must be made about the front-end bias tuning, which is not part of calibration but is nevertheless a key step in setting the instrument scientific performance. In order to satisfy tight mass and power constraints, power bias lines have been divided into four common-grounded power groups, with no bias voltage readouts. Only the total drain current flowing through the front-end amplifiers is measured and is available in the housekeeping telemetry. This design has important implications on front-end bias tuning, which depends critically on the satellite electrical and thermal configuration. Therefore front-end bias tuning has been repeated at all integration stages, and will also be repeated in flight before the start of nominal operations. Details about bias tuning performed at the various integration levels can be found in Davis et al. (2009), Varis et al. (2009), Villa et al. (2009) and Cuttaia et al. (2009).

## 4. Instrument-level cryogenic environment and test setup

The LFI receivers and the integrated instrument were tested in 2006 at the Thales Alenia Space-Italia laboratories located in Vimodrone (Milano). Custom-designed cryofacilities were developed in order to reproduce as closely as possible flight-like thermal, electrical, and data interface conditions (Terenzi et al. 2009b). Table 2 compares the main expected flight thermal conditions with those reproduced during tests on individual receivers and on the integrated instrument.

As can be seen from the table, during the integrated instrument tests the temperature of the sky and reference

**Table 1.** Main instrument parameters and stages at which they have been / will be measured. In bodface we highlight calibration parameters defining the instrument scientific performance that are discussed in this paper.

Category	Parameters	Additional Reference	Individual radiometers	Integrated instrument	Satellite	In flight
<i>Bias tuning</i>	Front-end amplifiers	Cuttaia et al. (2009)	Y	Y	Y	Y
	Phase switches	Cuttaia et al. (2009)	Y	Y	Y	Y
<b>Calibration</b>						
<i>Basic calibration</i>	<b>Photometric calibration</b>	Villa et al. (2009)	Y	Y	Y	Y
	<b>Linearity</b>	Mennella et al. (2009)	Y	Y	N	N
	<b>Isolation</b>	Villa et al. (2009)	Y	Y	N	N
	In-band response	Zonca et al. (2009)	Y	N	N	N
<i>Noise performance</i>	<b>White noise</b>	Meinhold et al. (2009)	Y	Y	Y	Y
	<b>Knee frequency</b>	Meinhold et al. (2009)	Y	Y	Y	Y
	<b>1/f slope</b>	Meinhold et al. (2009)	Y	Y	Y	Y
<i>Susceptibility</i>	<b>Front-end temperature fluctuations</b>	Terenzi et al. (2009c)	Y	Y	Y	Y
	Back-end temperature fluctuations		Y	Y	N	N
	Front-end bias fluctuations		Y	Y	N	N

**Table 2.** Summary of main thermal conditions in flight and in the various testing facilities.

Temperatures	Flight	Receiver	Instr.
Sky	$\sim 3$ K	$\gtrsim 8$ K	$\gtrsim 18.5$ K
Ref.	$\sim 4.5$ K	$\gtrsim 8$ K	$\gtrsim 18.5$ K
Front-end	$\sim 20$ K	$\sim 20$ K	$\sim 26$ K
Back-end	$\sim 300$ K	$\sim 300$ K	$\sim 300$ K

loads was much higher than expected in flight (18.5 K vs. 3–4.5 K). To compensate for this, receiver-level tests were conducted with the sky and reference loads at two temperatures, one near flight, the other near 20 K (Villa et al. 2009). During the instrument-level tests, parameters dependent on the sky and reference load temperatures (such as the white noise sensitivity and the photometric calibration constant) could be extrapolated to flight conditions.

#### 4.1. Thermal setup

A schematic of the LFI cryo-facility with the main thermal interfaces is shown in Fig. 2. The LFI was installed face-down, with the feed-horns directed towards an ECCOSORB “sky-load” and the back-end unit resting upon a tilted support. The entire instrument was held in place by a counterweight system that allowed slight movements to compensate for thermal contractions during cooldown. The reference loads were mounted on a mechanical structure reproducing the HFI external interfaces inserted in the middle of the front-end unit.

We summarise here and in Tab. 3 the main characteristics and issues of the testing environment. Further details about the sky load thermal design can be found in Terenzi et al. (2009b).

**Front-end unit.** The front end unit and the LFI main frame were cooled by a large copper flange simulating the sorption cooler cold end interface. The flange was linked to the 20 K cooler by means of ten large copper braids. Its temperature was controlled by a PID controller, and was stable to  $\sim 35$  mK at temperatures  $\gtrsim 25.5$  K at the control stage. The thermal control system was also used

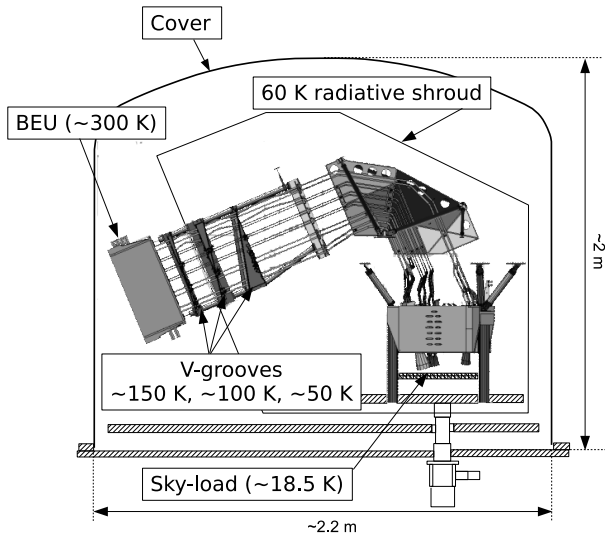


**Fig. 2.** LFI cryo-chamber facility. The LFI is mounted face-down with the feed horn array facing the eccosorb sky-load

in the susceptibility test to change the temperature of the front end in steps (see Sect 5.3).

**Sky load.** The sky load was thermally linked to the 20 K cooler through a gas heat switch that could be adjusted to obtain the necessary temperature steps during calibration tests. One of the sensors mounted in the central region of the load did not work correctly during the tests and results from the thermal modelling were used to detail its thermal behaviour.

**Reference loads.** The reference loads were installed on an aluminium structure thermally anchored to the 20 K cooler by means of high conductivity straps.

An upper plate held all 70 GHz loads, while the 30 and 44 GHz loads were attached to three individual flanges. Two thermometers on the bottom flange were used to measure and control the temperature of the whole structure. Five other sensors monitored the temperatures of the aluminum cases of the reference loads. The average temperature of the loads was around 22.1 K, with typical peak-to-peak stability of 80 mK.

**Radiative shroud.** The LFI was enclosed in a thermal shield intercepting parasitics and providing a cold radiative environment. The outer surface was highly reflective, while the inner surface was coated black to maximise radiative coupling. Two 50 K refrigerators cooled the thermal shield to temperatures in the range 43–70 K, depending on the distance to the cryocooler cold head, as measured by twelve diode sensors.

**Back-end unit.** The warm back-end unit was connected to a water circuit with temperature stabilised by a PID (Proportional, Integral, Derivative) controller; this stage suffered from diurnal temperature instabilities of the order of  $\sim 0.5$  K peak-to-peak. The effect of these temperature instabilities was visible in the total power voltage output from some detectors, but was almost completely removed by differencing.

**Table 3.** Summary of the main LFI cryo-facility thermal performance. The temperature stability listed in the second column refers to the measured peak-to-peak during one day.

	Avg. Temp. (K)	Stability (K)
Sky load	18–35	0.10
Focal plane unit	26	0.03
Reference loads	22	0.08
Back end unit	315	0.65

## 5. Measured calibration parameters and scientific performance

In this section we present the main calibration and performance parameters (refer to Table 1).

During the instrument-level test campaign we experienced two failures, one on the 70 GHz radiometer LFI18M-0 and the other on the 44 GHz radiometer LFI24M-0. The LFI18M-0 failure was caused by a phase switch that cracked during cooldown. At the end of the test campaign, just before instrument delivery to ESA, the radiometer LFI18M-0 was replaced with a flight spare. In the second case the problem was a defective electrical contact to the amplifier  $V_{g2}$  (gate 2 voltage) line, which was repaired after the end of the test. Subsequent room-temperature tests as well cryogenic ground satellite tests (Summer 2008) and in-flight calibration (Summer 2009) showed full functionality, confirming the successful repair of LFI18M-0 and LFI24M-0. Because these two radiometers were in a failed state during the test campaign, we generally show no results from them. The only exception is the calibrated noise per frequency channel reported in Table 6, where:

- for LFI18M-0, we assume the same noise parameters obtained for LFI18S-1; and
- for LFI24M-0, we use the noise parameters measured during single-receiver tests before integration into the instrument array.

### 5.1. Basic calibration

#### 5.1.1. Experimental setup

These parameters have been determined by means of tests in which the radiometric average voltage output,  $V_{out}$ , was recorded for various input antenna temperature levels,  $T_{in}$ . Although straightforward in principle, these tests required the following conditions in the experimental setup and in the measurement procedure in order to maximise the achieved accuracy in the recovered parameters:

- the sky load temperature distribution must be accurately known;
- temperature steps must be large enough (at least few Kelvin) to dominate over variations caused by  $1/f$  noise or other instabilities;
- the reference load temperature must remain stable during the change in the sky load temperature or, alternatively, variations must be taken into account in the data analysis especially in the determination of receiver isolation;



- data points must be acquired at multiple input temperatures to increase accuracy in estimating response linearity.

These conditions were all met during receiver-level tests in which several steps were obtained over a temperature span ranging from  $\sim 8$  K to  $\sim 30$  K and where the sky-load temperature distribution was very well known both experimentally and from thermal modelling (Terenzi et al. 2009a; Villa et al. 2009).

On the other hand, during instrument-level tests these conditions were not as well-met:

- the total number of available temperature controllers allowed us to place only three sensors on the sky load, one on the back metal plate, one on the side, and one on the tip of the central pyramid. The input temperature was then determined using the measurements from these three sensors in a dedicated thermal model of the sky load itself;
- the minimum and maximum temperatures that could be set without impacting the focal plane and reference load temperatures were 17.5 K and 30 K, half the range obtained during receiver-level tests;
- the time needed to change the sky load temperature few kelvin was large, of the order of several hours, because of its large thermal mass. This limited to three the number of temperature steps that could be performed in the available time.

The reduced temperature range and number of discrete temperatures that could be set precluded determination of the linearity factor. which was therefore excluded from the fit and constrained to  $\pm 1\%$  around the value found during calibration of individual receivers (see Sect. 5.1.2).<sup>3</sup>

Table 4 summarises temperatures for the three temperature steps considered in these tests. The sky load temperature (antenna temperature), has been determined from the sky load thermal model using temperature sensor data. The reference load temperature is a direct measurement converted into antenna temperature. Front-end and back-end unit temperatures are direct temperature sensor measurements averaged over all sensors.

**Table 4.** Main temperatures during basic calibration temperature steps.

Step #	$T_{\text{sky}}$ (K)	$T_{\text{ref}}$ (K)	$T_{\text{FEU}}$ (K)	$T_{\text{BEU}}$ (C)
1	22.05	22.34	26.40	37.53
2	28.96	22.20	26.45	37.48
3	32.91	22.32	26.40	37.67

<sup>3</sup> The slight compression found in the output of the 30 and 44 GHz receivers is caused by the back-end amplifier and diode, which worked at the same conditions both during both test campaigns.

### 5.1.2. Photometric calibration, noise temperature and linearity

Noise temperatures and calibration constants can be calculated by fitting the  $V_{\text{out}}(T_{\text{sky}})$  data with the most representative model (Daywitt 1989; Mennella et al. 2009):

$$V_{\text{out}} = \frac{G_0(T_{\text{sky}} + T_{\text{noise}})}{1 + b G_0(T_{\text{sky}} + T_{\text{noise}})} \quad (2)$$

where  $V_{\text{out}}$  is the voltage output,  $T_{\text{sky}}$  is the sky load input antenna temperature,  $T_{\text{noise}}$  is the noise temperature,  $G_0$  is the photometric calibration constant in the limit of linear response, and  $b$  is the nonlinearity parameter. For perfectly linear receivers  $b = 0$ .

In Table 8 we summarise the best-fit parameters obtained for all the LFI detectors. The nonlinearity parameter  $b$  for the 70 GHz receivers is  $\lesssim 10^{-3}$ , consistent with zero within the measurement uncertainty. The 30 and 44 GHz receivers show some compression at high input temperatures. This nonlinearity arises from the back-end RF amplification stage and detector diode, which show compression down to very low input powers. The nonlinear response has been thoroughly tested both on the individual back end modules (Mennella et al. 2009) and during the RCA calibration campaign (Villa et al. 2009) and has been shown to fit well Eq. (2).

### 5.1.3. Isolation

Isolation was estimated from the average radiometer voltage outputs,  $V_{\text{sky}}$  and  $V_{\text{ref}}$ , at the two extreme sky load temperatures (Steps 1 and 3 in Table 4)<sup>4</sup>. Equations used to calculate isolation values and uncertainties are reported in Appendix B.

In Fig. 3 we summarise the measured isolation for all detectors and provide a comparison with similar measurements performed on individual receiver chains. The results show large uncertainties in isolation measured during instrument-level tests, caused by  $1/f$  noise instabilities in the total power datastreams that were not negligible in the time span between the various temperature steps that was of the order of few days.

Apart from the limitations given by the measurement setup, the results show that isolation lies in the range  $-10$  dB to  $-20$  dB, which is globally within the requirement of  $-13$  dB.

## 5.2. Noise properties

The pseudo-correlation design of the Planck-LFI receivers has been optimised to minimise the effects of  $1/f$  gain variations in the radiometers.

The white noise sensitivity of the receivers is essentially independent of the reference load temperature level (Seiffert et al. 2002) and can be written, in its most general form, as follows:

$$\Delta T_{\text{rms}} = K \frac{T_{\text{sky}} + T_{\text{noise}}}{\sqrt{\beta}} \quad (3)$$

<sup>4</sup> The test can be conducted, in principle, also by changing the reference load temperature. In the instrument cryofacility, however, this was not possible because only the sky load temperature could be controlled.

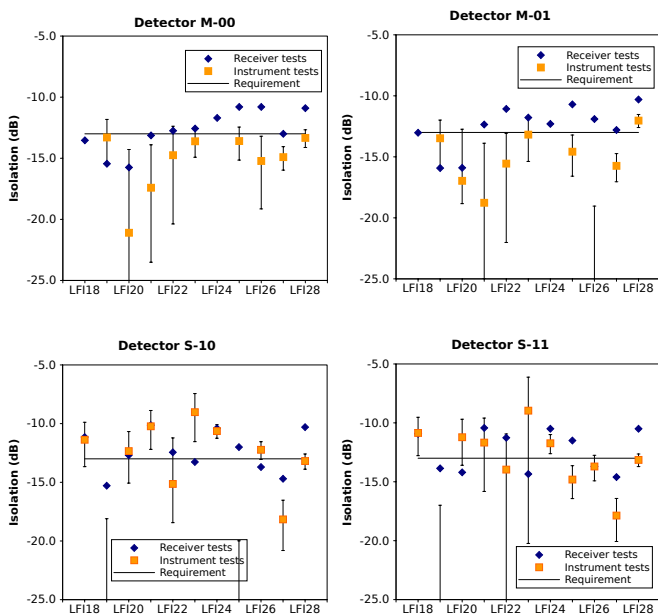


**Fig. 3.** Summary of measured isolation compared with the same measurements performed at receiver level (Villa et al. 2009).

where  $\beta$  is the receiver bandwidth,  $\Delta T_{\text{rms}}$  is the white noise sensitivity per unit integration time, and  $K$  is a constant.

For data obtained from a single diode output,  $K = 1$  for unswitched data and  $K = 2$  for differenced data. The factor of 2 for differenced data is the product of one  $\sqrt{2}$  from the difference and another  $\sqrt{2}$  from the halving of the sky integration time. When we average the two (calibrated) outputs of each radiometer we gain back a factor  $\sqrt{2}$ , so that the final radiometer sensitivity is given by Eq. (3) with  $K = \sqrt{2}$ .

Fig. 4 shows the effectiveness of the LFI pseudo-correlation design (see Meinhold et al. 2009). The  $1/f$  knee frequency is reduced, after differencing, by more than three orders of magnitude, and the white noise sensitivity scales almost perfectly with the three values of the constant  $K$ . The following terminology is used in the figure:

- *Total power data*: datastreams acquired without operating the phase switch;
- *Modulated data*: datastreams acquired in nominal, switching conditions before taking the difference in Eq. 1;
- *Diode differenced data*: differenced datastreams for each diode;
- *Radiometer differenced data*: datastreams obtained from a weighted average of the two diode differenced datastreams for each radiometer (see Eq. E.2).

### 5.2.1. Overview of main noise parameters

If we consider a typical differenced data noise power spectrum,  $P(f)$ , we can identify three main characteristics:

1. the white noise plateau, where  $P(f) \sim \sigma^2$ . The white noise sensitivity is given by  $\sigma$  (in units of  $\text{K s}^{1/2}$ ), and

the noise effective bandwidth by:

$$\beta = \frac{(KV_{\text{DC}}/\sigma_V)^2}{[1 + bG_0(T_{\text{sky}} + T_{\text{noise}})]^2}, \quad (4)$$

where  $V_{\text{DC}}$  is the voltage DC level,  $\sigma_V$  the uncalibrated white noise sensitivity and the term in square brackets represents the effect of compressed voltage output (see Appendix C);

2. the  $1/f$  noise tail, characterised by a power spectrum  $P(f) \sim \sigma^2(f/f_k)^{-\alpha}$  described by two parameters: the knee frequency,  $f_k$ , defined as the frequency where the  $1/f$  and white noise contribute equally, and the slope  $\alpha$ ;
3. spurious frequency spikes. These are a common-mode additive effect caused by interference between scientific and housekeeping data in the analog circuits of the data acquisition electronics box (see Sect. 5.2.5).

### 5.2.2. Test experimental conditions

The test used to determine instrument noise was a long duration (2 days) acquisition during which the instrument ran undisturbed in its nominal mode. Target temperatures were set at  $T_{\text{sky}} = 19 \text{ K}$  and  $T_{\text{ref}} = 22 \text{ K}$ . The front-end unit was at  $26 \text{ K}$ , maintained stable to  $\pm 10 \text{ mK}$ .

The most relevant instabilities were a  $0.5 \text{ K}$  peak-to-peak 24-hour fluctuation in the back-end temperature and a  $200 \text{ mK}$  drift in the reference load temperature caused by a leakage in the gas gap thermal switch that was refilled during the last part of the acquisition (see Fig. 5).

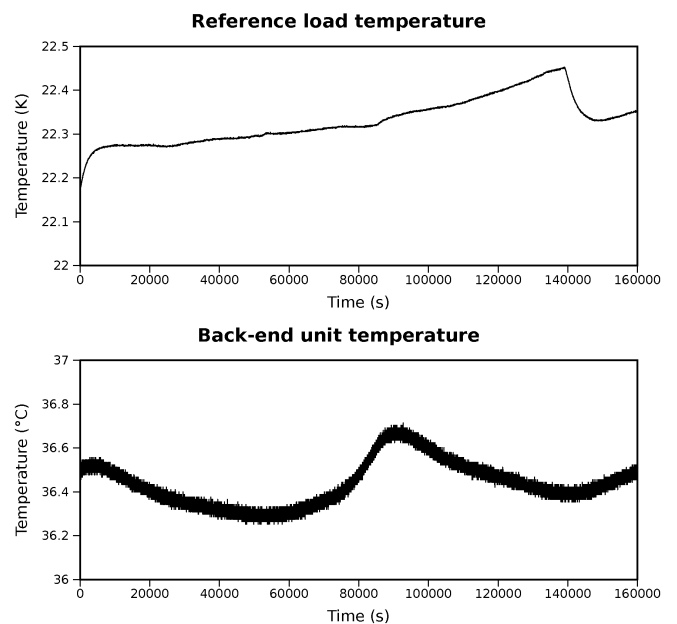


**Fig. 5.** Thermal instabilities during the long duration acquisition. *Top*: drift in the reference load temperature caused by leakage in the gas cap thermal switch. The drop towards the end of the test coincides with refill of the thermal switch. *Bottom*: 24-hr back-end temperature fluctuation.

The effect of the reference load temperature variation was clearly identified in the differential radiometric output

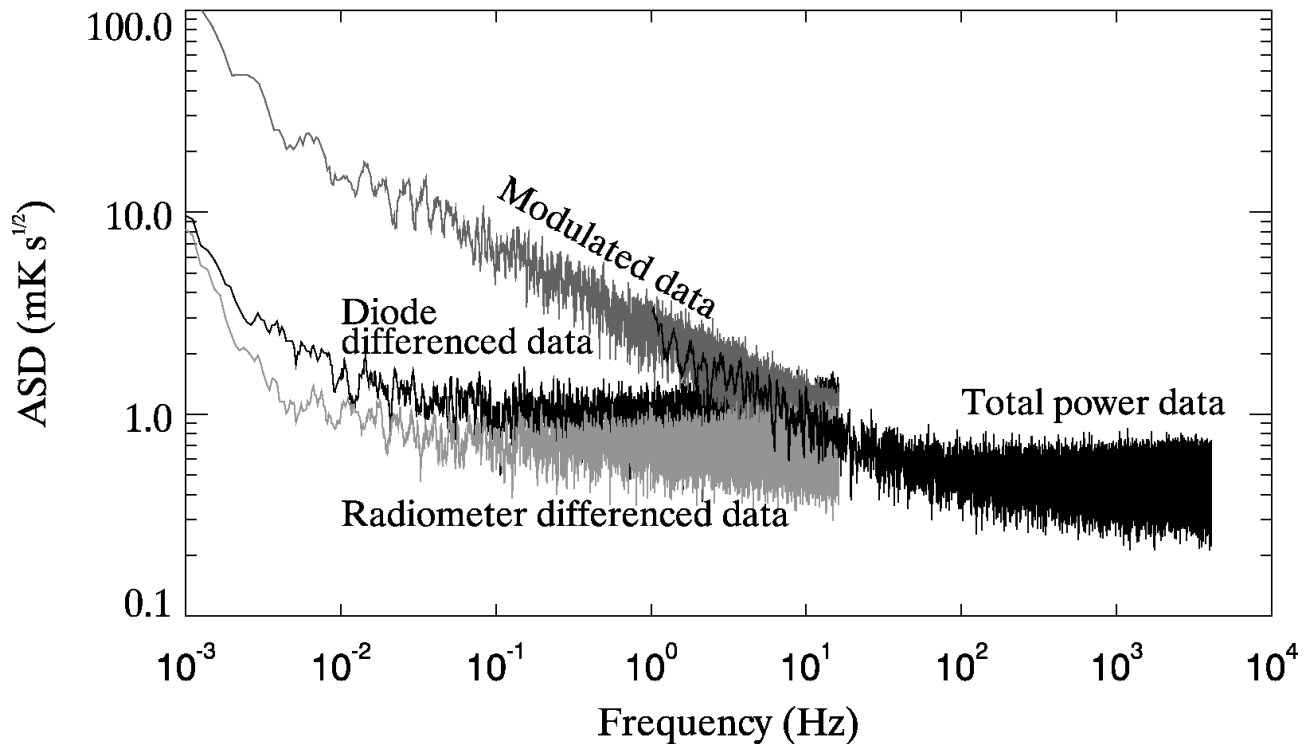


**Fig. 4.** Amplitude spectral densities of unswitched and differenced data streams. The pseudo-correlation differential design reduces the  $1/f$  knee frequency by three orders of magnitude. The white noise level scales almost perfectly with  $K$ .

(see Fig. 6) and removed from the radiometer data before differencing. The effect of the back-end temperature was removed by correlating the radiometric output with temperature sensor measurements.

### 5.2.3. White noise sensitivity and noise effective bandwidth

There are four sources of the white noise that determines the final sensitivity: (i) the input sky signal; (ii) the RF part of the receiver (active components and resistive losses); (iii) the back-end electronics after the detector diode<sup>5</sup>; and (iv) signal quantisation performed in the digital processing unit.

Signal quantisation can increase significantly the noise level if  $\sigma/q \lesssim 1$ , where  $q$  represents the quantisation step and  $\sigma$  the noise level before quantisation. Previous optimisation studies (Maris et al. 2003) have shown that a quantisation ratio  $\sigma/q \sim 2$  is enough to satisfy telemetry requirements without significantly increasing the noise level. This has been verified during calibration tests using the so-called “calibration channel”, i.e., a data channel containing about 15 minutes per day of unquantised data from each detector. The use of the calibration channel allowed a comparison between the white noise level before and after quantisation and compression for each detector. Table 9 summarises these results and shows that digital quantisation caused an increase in the signal white noise less than 1%.

<sup>5</sup> The additional noise introduced by the analog electronics is generally negligible compared to the intrinsic noise of the receiver, and its impact was further mitigated by the variable gain stage after the diode.

The white noise effective bandwidth calculated according to Eq. (4) is reported in Fig. 7. Our results indicate that the noise effective bandwidth is smaller than the requirement by 20%, 50%, and 10% at 30, 44, and 70 GHz, respectively. Non-idealities in the in-band response (ripples) causing bandwidth narrowing are discussed in Zonca et al. (2009).

It is useful to extrapolate these results to the expected in-flight sensitivity with the instrument at the nominal temperature of 20 K and observing a sky signal of  $\sim 2.73$  K in thermodynamic temperature. This estimate has been performed in two different ways. The first uses measured noise effective bandwidths and noise temperatures in the radiometer equation, Eq. (3). The second starts from measured uncalibrated noise, which is then calibrated in temperature units, corrected for the different focal plane temperature in test conditions, and extrapolated to  $\sim 2.73$  K input using the radiometric response equation, Eq (2). The details of the extrapolation are given in Appendix D.

Table 5 gives the sensitivity per radiometer estimated according to the two procedures. The sensitivity per radiometer has been obtained using a weighted noise average from the two detectors of each radiometer (see Appendix E). Because radiometers LFI18M-0 and LFI24M-0 were not working during the tests, we have estimated the sensitivity per frequency channel considering the white noise sensitivity of LFI24M-0 (that was later repaired) measured during receiver-level tests while for LFI18M-0 (that was later replaced with a spare unit) we have assumed the same sensitivity of LFI18S-1. Further details about white noise sensitivity of individual detectors are reported in Meinhold et al. (2009).

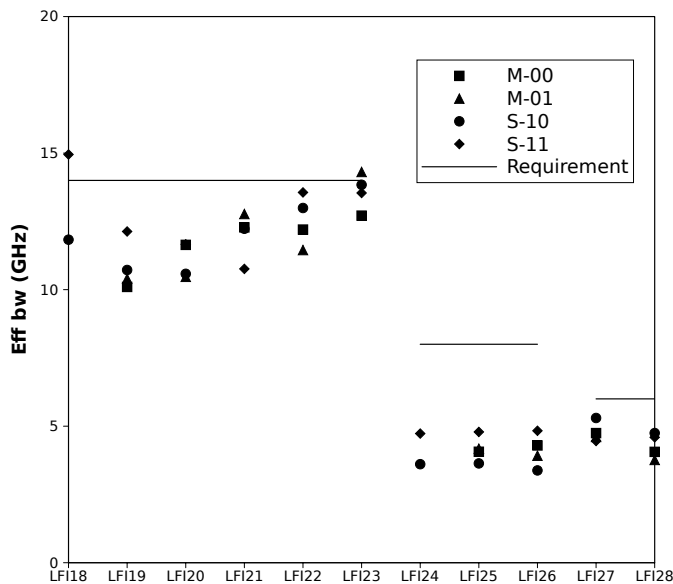


**Fig. 7.** Noise effective bandwidths calculated during RAA measurements. The three lines indicate the 70 GHz, 44 GHz and 30 GHz requirements.

**Table 5.** Calibrated white noise sensitivities in  $\mu\text{K s}^{1/2}$  per radiometer extrapolated at CMB input using the two methods outlined above and detailed in Appendix D.

From uncalib. noise			From radiom. equation		
	M-0	S-1		M-0	S-1
<b>70 GHz</b>			<b>70 GHz</b>		
LFI18	468	468	LFI18	450	450
LFI19	546	522	LFI19	482	466
LFI20	574	593	LFI20	498	511
LFI21	424	530	LFI21	381	496
LFI22	454	463	LFI22	428	410
LFI23	502	635	LFI23	453	419
<b>44 GHz</b>			<b>44 GHz</b>		
LFI24	372	447	LFI24	404	407
LFI25	501	492	LFI25	451	462
LFI26	398	392	LFI26	455	428
<b>30 GHz</b>			<b>30 GHz</b>		
LFI27	241	288	LFI27	311	320
LFI28	315	251	LFI28	305	268

The sensitivity per frequency channel estimated according the two procedures and compared with the LFI requirement is shown in Table 6.

#### 5.2.4. $1/f$ noise parameters

The  $1/f$  noise properties of the LFI differenced data have been better determined during instrument-level than receiver-level tests for two reasons: (i) the test performed in this phase has been the longest in all the test campaign, and (ii) because of the better temperature stability, especially compared to the 70 GHz receivers cryofacility (Villa et al. 2009).

best fit with two  $1/f$  components. Being a second-order correction we limit, in this paper, to results obtained with

**Table 6.** Calibrated white noise sensitivities in  $\mu\text{K s}^{1/2}$  per frequency channel extrapolated at CMB input using the two methods outlined above and detailed in Appendix D. The third column reports the LFI requirement.

	Meas. noise	Rad. eq.	Req.
70 GHz	146	130	105
44 GHz	174	177	113
30 GHz	135	149	116

**Table 7.** Summary of knee frequency and slope for all LFI detectors.

	$f_{\text{knee}}$ (mHz)			
	M-00	M-01	S-10	S-11
<b>70 GHz</b>				
LFI18	...	...	61	59
LFI19	25	32	27	37
LFI20	21	19	23	28
LFI21	28	30	41	38
LFI22	46	39	41	76
LFI23	30	31	58	75
<b>44 GHz</b>				
LFI24	...	...	39	46
LFI25	31	31	21	30
LFI26	61	61	61	14
<b>30 GHz</b>				
LFI27	30	30	27	26
LFI28	37	31	37	39
	slope			
	M-00	M-01	S-10	S-11
<b>70 GHz</b>				
LFI18	...	...	-1.12	-1.12
LFI19	-1.27	-1.22	-1.11	-1.02
LFI20	-1.47	-1.64	-1.27	-1.24
LFI21	-1.48	-1.61	-1.15	-1.17
LFI22	-1.18	-1.26	-1.19	-1.01
LFI23	-1.11	-1.19	-1.15	-1.12
<b>44 GHz</b>				
LFI24	...	...	-1.06	-1.11
LFI25	-1.07	-1.03	-1.10	-1.00
LFI26	-1.01	-1.01	-1.05	-1.55
<b>30 GHz</b>				
LFI27	-1.06	-1.13	-1.25	-1.13
LFI28	-0.94	-0.93	-1.07	-1.06

the simple model that Results, summarised in Table 7, show very good  $1/f$  noise stability of the LFI receivers, almost all with a knee frequency well below the required 50 mHz.

#### 5.2.5. Spurious frequency spikes

During the FM test campaign we found unwanted frequency spikes in the radiometric data at frequencies of the order of few hertz. The source of the problem was recognised to be in the backend data acquisition electronics box, where unexpected crosstalk between the circuits handling house-keeping and radiometric data affected the radiometer voltage output downstream of the detector diode.

This is shown clearly in Fig. 8, which shows spectra of unswitched data acquired from the 70 GHz detec-



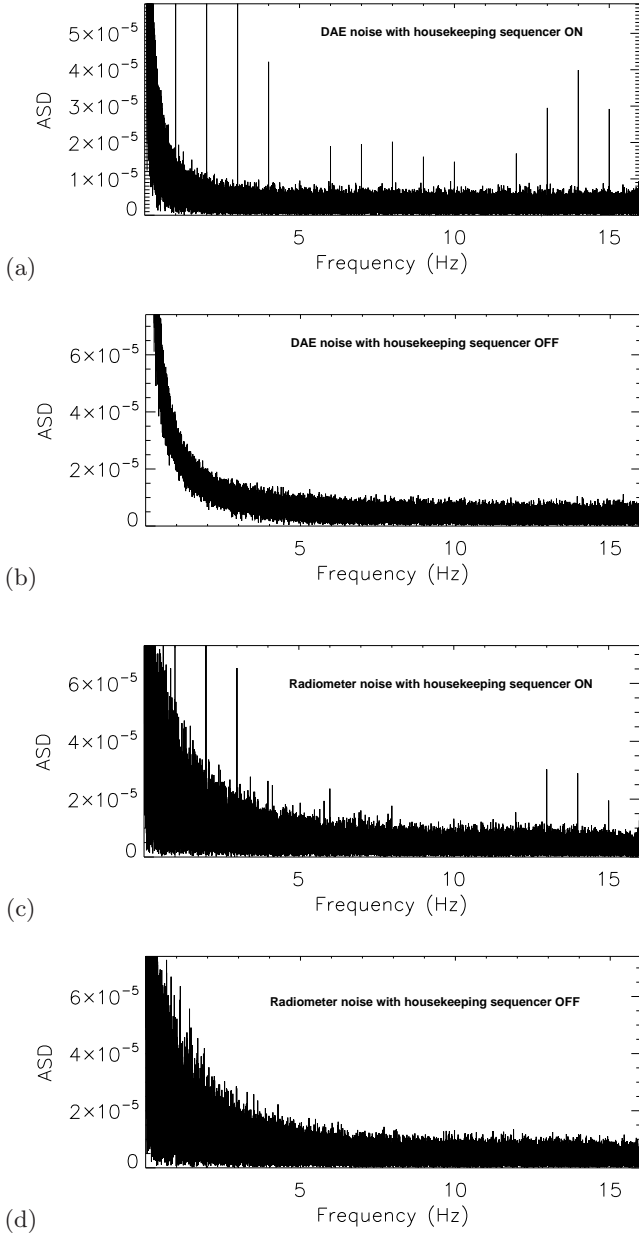


**Fig. 8.** DAE-only and radiometer noise amplitude density spectra in  $V/\sqrt{\text{Hz}}$  (from LFI18S-10 unswitched data) with and without activation of the housekeeping acquisition. These data show clearly that the source of the disturbance is in the data acquisition electronics box and is correlated with the status of the housekeeping data acquisition.

tor LFI18S-10 with the housekeeping data acquisition activated and deactivated.

Because the disturbance is added to receiver signal at the end of the radiometric chain it acts as a common mode effect on both the sky and reference load data so that its effect in differenced data is reduced by several orders of magnitude bringing it well below the radiometer noise level.

Further analysis of these spikes has shown that the disturbance is synchronized in time. By binning the data synchronously we obtain a template of the disturbance, which allows its removal in time-domain (Meinhold et al. 2009).

The feasibility of this approach has been proven with data acquired during the full satellite test campaign in Liege, Belgium during July and August, 2008.

Therefore, because the only way to eliminate the disturbance *in hardware* would be to operate the instrument without any housekeeping information, our baseline approach is that, if necessary, the residual effect will be removed from the data in time domain after measuring the disturbance shape from the flight data.

### 5.3. Radiometric susceptibility to front-end temperature instabilities

Thermal fluctuations in the receivers result in gain changes in the amplifiers and noise changes in the (slightly emissive) passive components (horns, OMTs, waveguides). These changes mimic the effect of changes in sky emission, especially at fluctuation frequencies near the satellite spin frequency. The most important source of temperature fluctuations for LFI is the sorption cooler (Bhandari et al. 2004; Wade et al. 2000).

For small temperature fluctuations in the focal plane the radiometric response is linear (Seiffert et al. 2002; Terenzi et al. 2009c), so the spurious antenna temperature fluctuation in the differential receiver output can be written as:

$$\delta T_{\text{out}} = f_{\text{trans}} \delta T_{\text{phys}}. \quad (5)$$

Transfer function  $f_{\text{trans}}$  can be estimated analytically from the differential power output given in Eq. (1):

$$f_{\text{trans}} = \frac{\partial p_{\text{out}}}{\partial T_{\text{phys}}} \left( \frac{\partial p_{\text{out}}}{\partial T_{\text{sky}}} \right)^{-1}. \quad (6)$$

The analytical form of  $f_{\text{trans}}$  (discussed in detail in Terenzi et al. 2009c) depends primarily on the front-end amplifier susceptibility parameters,  $\partial G/\partial T_{\text{phys}}$  and  $\partial T_{\text{noise}}/\partial T_{\text{phys}}$  as well as on other instrument and boundary condition parameters such as the insertion loss of passive components and the sky input temperature.

If we consider the systematic error budget in Bersanelli et al. (2009), it is possible to derive a requirement for the radiometric transfer function,  $f_{\text{trans}} \lesssim 0.1$ , in order to maintain the final peak-to-peak error per pixel  $\lesssim 1\mu\text{K}$  (see Appendix F). During instrument-level calibration activities dedicated tests were run to estimate  $f_{\text{trans}}$  and compare it with theoretical estimates and similar tests performed on individual receivers.

#### 5.3.1. Experimental setup

During this test the focal plane temperature was varied in steps between between 27 and 34K. The sky and reference load temperatures were  $T_{\text{sky}} = 35 \pm 0.01\text{K}$  and  $T_{\text{ref}} = 23.7 \pm 0.01\text{K}$ . The reference load temperature showed a non-negligible coupling with the focal plane temperature (as shown in Fig 9) so that the effect of this variation had to be removed from the data before calculating the thermal transfer function.

Although the test lasted more than 24 hours, it was difficult to reach a clean steady state plateau after each step because of the large thermal mass of the instrument. Furthermore, for some detectors the bias tuning was not

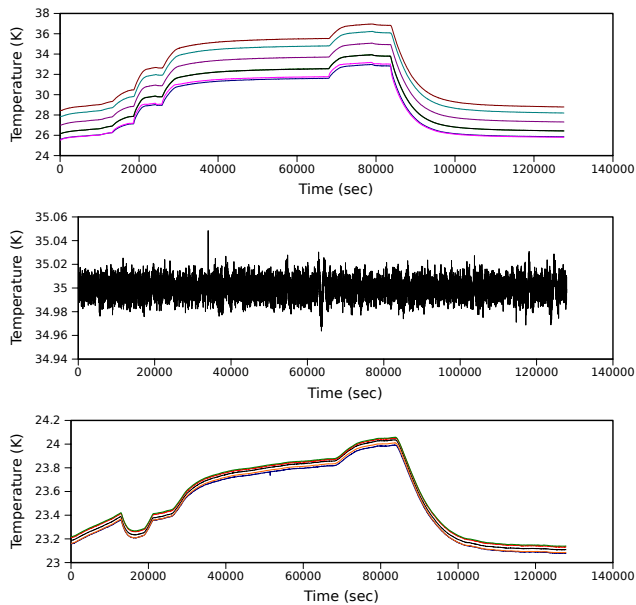


**Fig. 9.** Behaviour of focal plane (top), sky load (middle) and reference load (bottom) temperatures during the thermal susceptibility tests.

yet optimised, so that only data from a subset of detectors could be compared with similar measurements performed at receiver-level.

In Fig. 10 we summarise our results by comparing predicted and measured transfer functions for the tested detectors. Predicted transfer functions have been calculated using the list of parameters provided in Appendix G, derived from receiver-level tests. In the same figure we also plot the thermal susceptibility requirement rescaled at the experimental test conditions with a scale factor given by the ratio

$$f_{\text{trans}}(\text{ground})/f_{\text{trans}}(\text{flight}), \quad (7)$$

where  $f_{\text{trans}}$  has been calculated using Eq. (5) in ground and flight conditions from sky, reference-load and focal plane temperatures.

Fig. 10 shows that transfer functions measured during instrument-level tests are compliant with scientific requirements and reflect theoretical predictions, with the exception of LFI22 and LFI23, which were more susceptible to front-end temperature fluctuations than expected. In general, results from the instrument test campaign confirm design expectations, and suggest that the level of temperature instabilities in the focal plane will not represent a significant source of systematic errors in the final scientific products. This has been further verified during satellite thermal-vacuum tests conducted with the flight model sorption cooler (see Sect. 6.4).

## 6. Comparison with satellite level test results

The final cryogenic ground test campaign was conducted at the Centre Spatiale de Liège (CSL) with the LFI and the HFI integrated on board Planck. To reproduce flight temperature conditions, the satellite was enclosed in an outer cryochamber cooled to liquid nitrogen temperatures, and surrounded an inner thermal shield at  $\sim 20$  K. An

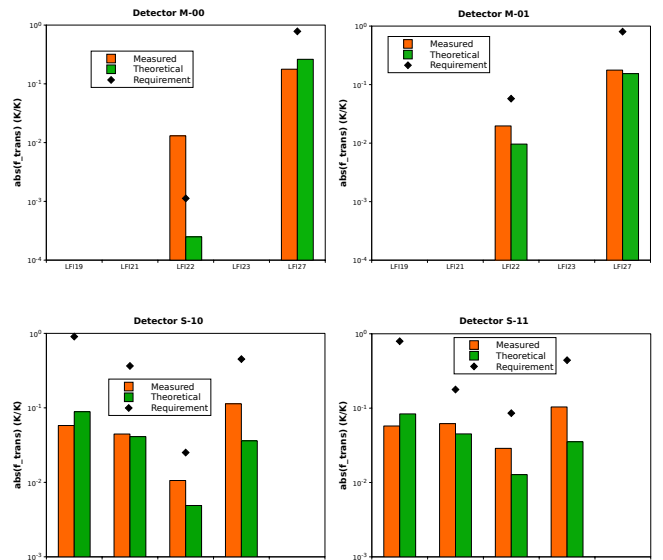


**Fig. 10.** Measured and predicted radiometric thermal transfer functions, with the scientific requirement rescaled at the experimental conditions of the test. The comparison is possible only for the subset of radiometers that was tuned at the time of this test.

ECCOSORB load cooled to 4.5 K was placed between the secondary mirror and the feed horns to simulate the cold sky. For the first time, the LFI focal plane was cooled to 20 K by the sorption cooler, and the reference loads were cooled to  $\sim 4$  K by the 4 K cooler.

During the CSL tests we verified instrument functionality, tuned front-end biases and back-end electronics, and assessed scientific performance in the closest conditions to flight attainable on the ground. Front-end bias tuning made use of the ability of the 4 K cooler system to provide several different stable temperatures to the reference loads in the range 24 K down to the nominal 4 K (Cuttaia et al. 2009).

A detailed description of satellite-level tests is outside the scope of this paper; here we will focus on the comparison of the main performance parameters measured during instrument and satellite tests, and show that despite differences in test conditions the overall behaviour was reproduced.

### 6.1. White noise sensitivity

Calibrated white noise sensitivities were determined during satellite-level tests by exploiting a  $\sim 80$  mK variation of the sky load temperature caused by the periodic helium refills of the chamber. This variation allowed us to estimate the photometric calibration constant by correlating the differenced voltage datastream  $\delta V(t)$  from each detector with the sky load temperature  $T_{\text{sky}}^{\text{ant}}(t)$  (in antenna temperature units).

To extrapolate the calibrated sensitivity from the 4.5 K input temperature in the test to flight conditions we calculated the ratio:

$$\frac{\Delta T_{\text{rms}}(T_{\text{sky}}^{\text{flight}})}{\Delta T_{\text{rms}}(T_{\text{sky}}^{\text{CSL}})} = \frac{(T_{\text{sky}}^{\text{flight}} + T_{\text{noise}})}{(T_{\text{sky}}^{\text{CSL}} + T_{\text{noise}})} \quad (8)$$

using the noise temperature found from the non-linear model fit from the receiver-level test campaign (Villa et al. 2009). This ratio ranges from a minimum of  $\sim 0.96$  to a maximum of  $\sim 0.98$ . Exact values for each detector are not reported here for simplicity.

In Fig. 11 we summarise graphically the in-flight sensitivity estimates from the three tests. In the following plots the sensitivity values are provided with error bars, with the following meanings:

- error bars in sensitivities estimated from satellite-level data represent the statistical error in the calibration constants calculated from the various temperature jumps and propagated through the sensitivity formulas. They represent genuine statistical uncertainties;
- error bars in sensitivities estimated from receiver and instrument level tests data represent the uncertainty coming from the calculation performed according to the two different methods described in Sect. 5.2.3 and Appendix D. In this case error bars do not have specific statistical significance, but nevertheless provide an indication of uncertainties in the estimate.

Fig. 11 shows that the in-flight sensitivity lies between the requirement and twice the goal levels for the 30 and 70 GHz receivers, and at about twice the goal for the 44 GHz receivers. The agreement between values extrapolated from the three test campaigns is very good, apart from two noticeable outliers, LFI21S-1 and LFI24M-0, which showed a higher noise level during satellite level tests. Investigation showed that this anomaly was due to incorrect bias voltages on the front-end devices during the test.

After a thorough bias tuning activity conducted during in flight calibration (see Cuttaia et al. 2009) a new bias configuration was found that normalised the white noise sensitivity of these two receivers, as expected. A full description of the in-flight calibration results and scientific performance will be given in a forthcoming dedicated paper.

## 6.2. Noise stability

Receiver noise stability during satellite-level tests was determined from stable data acquisitions lasting several hours with the instruments in their tuned and nominal conditions. Fig. 12 summarises  $1/f$  knee frequencies measured at instrument and satellite levels compared with the 50 mHz requirement, and shows that the noise stability of all channels is within requirements, with the single marginal exception of LFI23S-11. The slope ranged from a minimum of 0.8 to a maximum of 1.7.

There was a substantial improvement in noise stability during satellite-level tests compared to instrument-level tests, in some cases with a reduction in knee frequency of more than a factor of 2. This can partly be explained by the almost perfect signal input balance achieved in the CSL cryo-facility (much less than 1 K compared to the  $\sim 3$  K obtained in the instrument cryo-facility). Some of the improvement was also expected because of the much better thermal stability of the CSL facility. In particular fluctuations of the sky and reference loads in CSL were about two order of magnitudes less than those in the instrument facility (see Table 3). Because the highly balanced input achieved in CSL will not be reproduced in flight we ex-

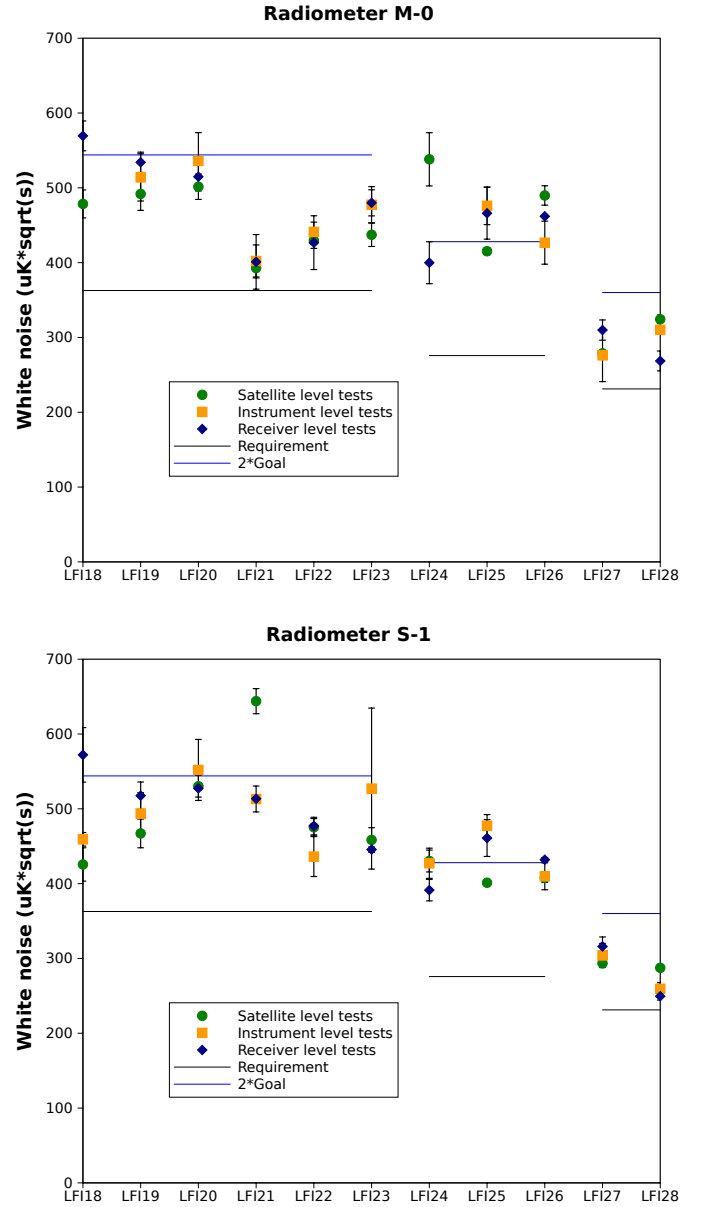


**Fig. 11.** Summary of in-flight sensitivities per radiometer estimated from receiver, instrument and satellite level test campaigns.

pect that the flight knee frequencies will be slightly higher (although similar) compared to those measured in CSL.

## 6.3. Isolation

Isolation (see Eq. (B.3)) was measured during the satellite tests by changing the reference load temperature by 3.5 K. Fig. 13 compares isolation measured during receiver- and satellite-level tests. Several channels exceed the  $-13$  dB requirement; a few are marginally below. One channel, LFI21S-1, showed poor isolation of only  $-7$  dB. This result is consistent with the high value of the calibrated white noise measured for this channel (see Sect. 6.1), supporting the hypothesis of non-optimal biasing of that channel.

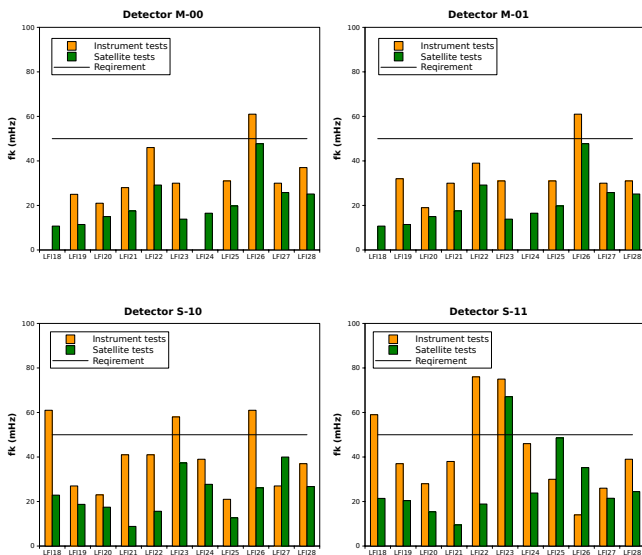


**Fig. 12.** Summary of  $1/f$  knee frequencies measured at instrument and satellite levels.

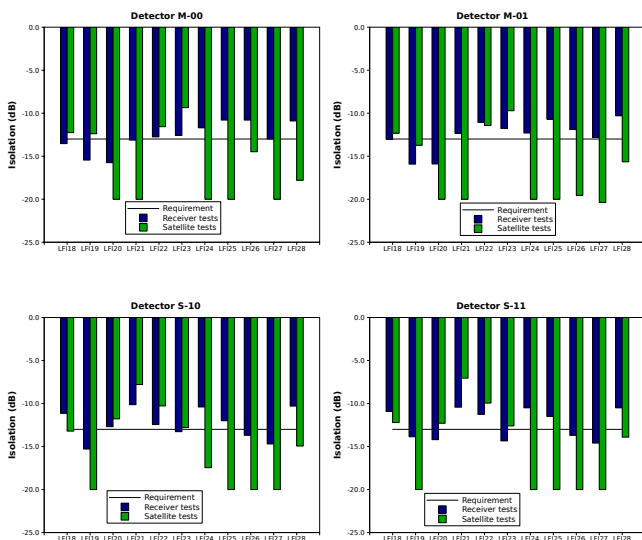


**Fig. 13.** Summary of isolation measured at receiver and satellite levels.

#### 6.4. Thermal susceptibility

As mentioned in Sect. 4.3, the most important source of temperature fluctuations in the LFI focal plane is the sorption cooler. The satellite-level test provided the first opportunity to measure the performance of the full Planck thermal system. Fluctuations at the interface between the sorption cooler and the LFI were measured to be about 100 mK peak-to-peak. Using methods described in (Mennella et al. 2002), we calculate that the effect of these fluctuations will be less than  $1 \mu\text{K}$  per pixel in the maps, in line with the scientific requirements outlined in Bersanelli et al. (2009).

## 7. Conclusions

The LFI was integrated and tested in thermo-vacuum conditions at the Thales Alenia Space Italia laboratories, lo-

cated in Vimodrone (Milano), during the summer of 2006. The test goals were a wide characterisation and calibration of the instrument, ranging from functionality to scientific performance assessment.

The LFI was fully functional, apart from two failed components in LFI18M-0 and LFI24M-0 that have been fixed (one replaced and the other repaired) after the cryogenic test campaign, recovering full functionality.

Measured instrument parameters are consistent with measurements performed on individual receivers. In particular, the LFI shows excellent  $1/f$  stability and rejection of instrumental systematic effects. Although the very ambitious sensitivity goals have not been fully met, the measured performance makes LFI the most sensitive instrument of its kind, a factor of 2 to 3 better than WMAP<sup>6</sup> at the same frequencies. In particular at 70 GHz, near the minimum of the foreground emission for both temperature and polarisation anisotropy, the combination of sensitivity and angular resolution of LFI will provide a clean reconstruction of the temperature power spectrum up to  $\ell \sim 1400$  (Mandolesi et al. 2009).

After the instrument test campaign, the LFI was integrated with the HFI and the satellite. Between June and August 2008, Planck was tested at the Centre Spatial de Liège in flight-representative, thermo-vacuum conditions, and showed to be fully functional.

Planck was launched on May 14<sup>th</sup> from the Guyane Space Centre in Kourou and has reached its observation point, L2. In-flight testing and calibration is underway, and will provide the final instrument tuning and scientific performance assessment. After 17 years, Planck is nearly ready to start recording the first light in the Universe.

*Acknowledgements.* The Planck-LFI project is developed by an International Consortium lead by Italy and involving Canada, Finland, Germany, Norway, Spain, Switzerland, UK, USA. The Italian contribution to Planck is supported by the Italian Space Agency (ASI). The work in this paper has been supported by in the framework of the ASI-E2 phase of the Planck contract. The US Planck Project is supported by the NASA Science Mission Directorate. In Finland, the Planck LFI 70 GHz work was supported by the Finnish Funding Agency for Technology and Innovation (Tekes).

<sup>6</sup> Calculated on the final resolution element per unit integration time

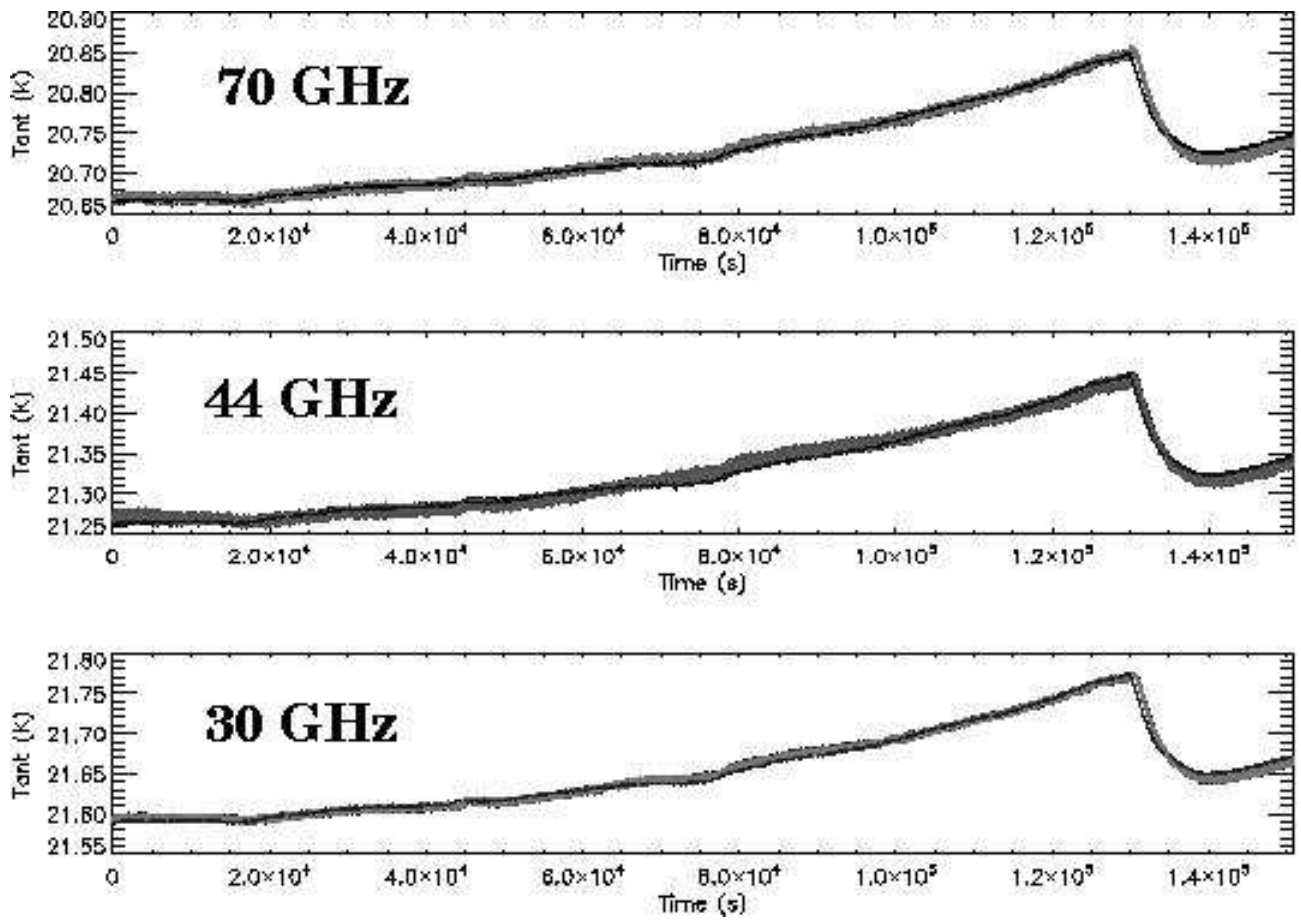


**Fig. 6.** Calibrated differential radiometric outputs (downsampled to 1 Hz) for all LFI detectors during the long duration test. Temperature sensor data in antenna temperature units are superimposed (thin black line) on the calibrated radiometric data.



**Table 8.** Best fit parameters obtained from the non linear fit of data acquired during instrument-level tests. Notice that the linearity factor was obtained by constraining it to  $\pm 1\%$  around the value found during calibration of individual receivers.(see Mennella et al. 2009)

Rec. ID	Param.	M-00	M-01	S-10	S-11
<b>LFI18</b>	$b$	...	...	$\lesssim 10^{-3}$	$\lesssim 10^{-3}$
	$G_0$ (V/K)	...	...	0.026	0.022
	$T_{\text{noise}}$ (K)	...	...	37.4	40.5
<b>LFI19</b>	$b$	$\lesssim 10^{-3}$	$\lesssim 10^{-3}$	$\lesssim 10^{-3}$	$\lesssim 10^{-3}$
	$G_0$ (V/K)	0.020	0.021	0.016	0.018
	$T_{\text{noise}}$ (K)	39.8	38.7	37.5	40.0
<b>LFI20</b>	$b$	$\lesssim 10^{-3}$	$\lesssim 10^{-3}$	$\lesssim 10^{-3}$	$\lesssim 10^{-3}$
	$G_0$ (V/K)	0.019	0.018	0.025	0.025
	$T_{\text{noise}}$ (K)	42.3	42.2	43.9	43.0
<b>LFI21</b>	$b$	$\lesssim 10^{-3}$	$\lesssim 10^{-3}$	$\lesssim 10^{-3}$	$\lesssim 10^{-3}$
	$G_0$ (V/K)	0.025	0.023	0.016	0.014
	$T_{\text{noise}}$ (K)	31.9	34.6	43.3	45.9
<b>LFI22</b>	$b$	$\lesssim 10^{-3}$	$\lesssim 10^{-3}$	$\lesssim 10^{-3}$	$\lesssim 10^{-3}$
	$G_0$ (V/K)	0.011	0.012	0.014	0.016
	$T_{\text{noise}}$ (K)	40.5	38.9	40.8	43.5
<b>LFI23</b>	$b$	$\lesssim 10^{-3}$	$\lesssim 10^{-3}$	$\lesssim 10^{-3}$	$\lesssim 10^{-3}$
	$G_0$ (V/K)	0.025	0.029	0.014	0.007
	$T_{\text{noise}}$ (K)	40.6	39.2	50.3	54.2
<b>LFI24</b>	$b$	...	...	1.43	1.43
	$G_0$ (V/K)	...	...	0.005	0.005
	$T_{\text{noise}}$ (K)	...	...	19.7	19.9
<b>LFI25</b>	$b$	1.21	1.16	0.79	1.00
	$G_0$ (V/K)	0.008	0.008	0.007	0.007
	$T_{\text{noise}}$ (K)	19.7	19.7	20.5	20.2
<b>LFI26</b>	$b$	1.07	1.40	0.93	1.21
	$G_0$ (V/K)	0.005	0.006	0.007	0.007
	$T_{\text{noise}}$ (K)	20.2	19.1	18.5	18.1
<b>LFI27</b>	$b$	0.12	0.12	0.12	0.14
	$G_0$ (V/K)	0.074	0.081	0.070	0.058
	$T_{\text{noise}}$ (K)	13.3	13.1	14.3	13.7
<b>LFI28</b>	$b$	0.19	0.16	0.19	0.19
	$G_0$ (V/K)	0.076	0.103	0.071	0.061
	$T_{\text{noise}}$ (K)	11.7	11.3	10.9	10.8

**Table 9.** Measured white noise spectral densities (in  $\mu\text{V}/\sqrt{\text{Hz}}$ ) before and after quantisation and compression for all detectors. No values are given for LFI26S-11, for which quantisation and compression parameters were set to wrong values because of a problem in the software optimisation procedure that was identified and solved after the calibration campaign.

	M-00			M-01			S-10			S-11		
	$\sigma$	$\sigma_q$	$\Delta$	$\sigma$	$\sigma_q$	$\Delta$	$\sigma$	$\sigma_q$	$\Delta$	$\sigma$	$\sigma_q$	$\Delta$
<b>70 GHz</b>												
LFI18	...	...	...	...	...	...	38.93	39.22	0.74%	31.07	31.39	1.02%
LFI19	33.50	33.68	0.55%	34.00	34.13	0.39%	25.68	25.85	0.63%	27.48	27.67	0.71%
LFI20	31.08	31.17	0.31%	31.20	31.37	0.54%	44.77	45.14	0.83%	41.95	42.23	0.67%
LFI21	33.77	33.94	0.51%	32.27	32.39	0.35%	26.50	26.67	0.62%	25.63	25.86	0.87%
LFI22	17.03	17.15	0.67%	19.29	19.41	0.61%	20.99	21.05	0.28%	23.94	24.06	0.49%
LFI23	37.84	38.01	0.44%	41.00	41.25	0.61%	23.76	24.01	1.04%	12.15	12.19	0.36%
<b>44 GHz</b>												
LFI24	...	...	...	...	...	...	5.95	5.97	0.25%	5.32	5.35	0.45%
LFI25	7.50	7.54	0.50%	7.53	7.55	0.30%	9.34	9.37	0.35%	6.93	6.96	0.43%
LFI26	6.04	6.06	0.32%	6.18	6.20	0.31%	8.81	8.84	0.28%	...	...	...
<b>30 GHz</b>												
LFI27	62.34	62.67	0.52%	65.62	65.97	0.53%	56.19	56.40	0.37%	52.48	52.59	0.22%
LFI28	52.96	53.27	0.59%	68.34	68.58	0.34%	46.77	46.94	0.35%	44.15	44.24	0.20%

## Appendix A: LFI receiver and channel naming convention

The various receivers are labelled LFI18 to LFI28, as shown in Fig. A.1. The radiometers connected to the two OMT arms are labelled M-0 (“main” OMT arm) and S-1 (“side” OMT arm), while the two output detectors from each radiometer are be labelled as 0 and 1. Therefore LFI18S-10, for example, refers to detector 0 of the side arm of receiver LFI18, and LFI24M-01 refers to detector 1 of the main arm of receiver LFI24.

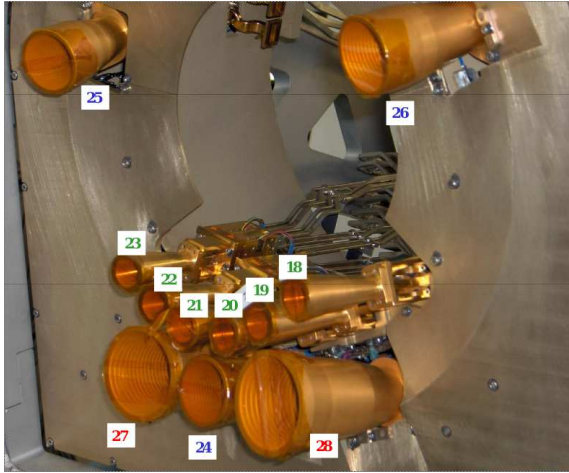


**Fig. A.1.** Feed horns in the LFI focal plane. Each feed horn is tagged by a label running from LFI18 to LFI28. LFI18 through LFI23 are 70 GHz receivers, LFI24 through LFI26 are 44 GHz receivers and LFI27, LFI28 are 30 GHz receivers.

## Appendix B: Receiver isolation: definition, scientific requirements and measurements

### B.1. Definition and requirement.

In Sect. 2 it is shown that the output of the LFI pseudo-correlation receivers is a sequence of sky and reference load signals alternating at twice the phase switch frequency. If the pseudo-correlator is not ideal, the separation after the second hybrid is not perfect and a certain level of mixing between the two signals will be present in the output. Typical limitations on isolation are (i) imperfect hybrid phase matching, (ii) front-end gain amplitude mismatch, and (iii) mismatch in the insertion loss in the two switch states (Seiffert et al. 2002).

A more general relationship representing the receiver power output can be written as:

$$p_{\text{out}} = aG_{\text{tot}}k\beta [(1 - \epsilon)T_{\text{sky}} + \epsilon T_{\text{ref}} + T_{\text{noise}} + r((1 - \epsilon)T_{\text{ref}} + \epsilon T_{\text{sky}} + T_{\text{noise}})] \quad (\text{B.1})$$

where the parameters  $\epsilon$  represents the degree of mixing or, in other words, deviation from ideal isolation.

Let us now imagine the receiver scanning the sky and therefore measuring a variation in the sky signal given by

the CMB,  $\Delta T_{\text{CMB}}$ . If we define  $r = \frac{T_{\text{sky}} + T_{\text{noise}}}{T_{\text{ref}} + T_{\text{noise}}}$  and develop Eq. (B.1) in series up to the first order in  $\epsilon$  we see that the differential power output is proportional to:

$$p_{\text{out}} \propto \Delta T_{\text{CMB}} (1 - \delta_{\text{iso}}) \quad (\text{B.2})$$

where  $\delta_{\text{iso}} = \frac{2T_{\text{noise}} + T_{\text{sky}} + T_{\text{ref}}}{T_{\text{noise}} + T_{\text{ref}}}\epsilon$ , which provides a useful relationship to estimate the requirement on the isolation,  $\epsilon_{\text{max}}$  given an acceptable level of  $\delta_{\text{iso}}^{\text{max}}$ .

If we assume 10% (corresponding to  $\delta_{\text{iso}}^{\text{max}} \sim 0.1$ ) as the maximum acceptable loss in the CMB signal due to imperfect isolation and consider typical values for the LFI receivers ( $T_{\text{ref}} = 4.5$  K and  $T_{\text{noise}}$  ranging from 10 to 30 K), we find  $\epsilon_{\text{max}} = 0.05$  equivalent to  $-13$  dB, which corresponds to the requirement for LFI receivers.

### B.2. Measurement.

If  $\Delta V_{\text{sky}}$  and  $\Delta V_{\text{ref}}$  are the voltage output variations induced by  $\Delta T = T_2 - T_1$ , then it is easy to see from Eq. (B.1) (with the approximation  $(1 - \epsilon) \simeq 1$ ) that:

$$\epsilon \simeq \frac{\Delta V_{\text{ref}}}{\Delta V_{\text{sky}} + \Delta V_{\text{ref}}}. \quad (\text{B.3})$$

If the reference load temperature is not perfectly stable but varies by an amount  $\Delta T_{\text{ref}}$  during the measurement, this can be corrected at first order if we know the photometric constant  $G_0$ . In this case Eq. (B.3) becomes:

$$\epsilon \simeq \frac{\Delta V_{\text{ref}} - G_0 \Delta T_{\text{ref}}}{\Delta V_{\text{sky}} + \Delta V_{\text{ref}} - G_0 \Delta T_{\text{ref}}}. \quad (\text{B.4})$$

Measuring the isolation accurately, however, is generally difficult and requires a very stable environment. In fact, any change in  $\Delta V_{\text{ref}}$  caused by other systematic fluctuations (e.g., temperature fluctuations,  $1/f$  noise fluctuations) will impact the isolation measurement causing an over- or under-estimation depending on the sign of the effect.

To estimate the accuracy in our isolation measurements, we have first calculated the uncertainty caused by a systematic error in the reference load voltage output,  $\Delta V_{\text{ref}}^{\text{sys}}$ . If we substitute in Eq. (B.4)  $\Delta V_{\text{ref}}$  with  $\Delta V_{\text{ref}} \pm \Delta V_{\text{ref}}^{\text{sys}}$  and develop at first order in  $\Delta V_{\text{ref}}^{\text{sys}}$ , we obtain

$$\epsilon \sim \epsilon_0 \mp \frac{\Delta V_{\text{sky}}}{\Delta V_{\text{sky}} + \Delta V_{\text{ref}} - G_0 \Delta T_{\text{ref}}} \Delta V_{\text{ref}}^{\text{sys}} \equiv \epsilon_0 \mp \delta\epsilon, \quad (\text{B.5})$$

where we indicate with  $\epsilon_0$  the isolation given by Eq. (B.4).

We estimated  $\delta\epsilon$  in our measurement conditions. Because the three temperature steps were implemented in about one day we have evaluated the total power signal stability on this timescale from a long-duration acquisition in which the instrument was left running undisturbed for about two days. For each detector datastream we have first removed spurious thermal fluctuations by correlation analysis with temperature sensor data then we calculated the peak-to-peak variation in the reference load datastream.

## Appendix C: Calculation of noise effective bandwidth

The well-known radiometer equation applied to the output of a single diode in the Planck LFI receivers links the

white noise sensitivity to sky and noise temperatures and the receiver bandwidth. It reads (Seiffert et al. 2002):

$$\delta T_{\text{rms}} = 2 \frac{T_{\text{sky}} + T_{\text{noise}}}{\sqrt{\beta}}. \quad (\text{C.1})$$

In the case of linear response, i.e. if  $V_{\text{out}} = G \times (T_{\text{sky}} + T_{\text{noise}})$  (where  $G$  represents the photometric calibration constant) we can write Eq. (C.1) in its most useful uncalibrated form:

$$\delta V_{\text{rms}} = 2 \frac{V_{\text{out}}}{\sqrt{\beta}}, \quad (\text{C.2})$$

which is commonly used to estimate the receiver bandwidth,  $\beta$ , from a simple measurement of the receiver DC output and white noise level, i.e.:

$$\tilde{\beta} = 4 \left( \frac{V_{\text{out}}}{\delta V_{\text{rms}}} \right)^2. \quad (\text{C.3})$$

If the response is linear and if the noise is purely radiometric (i.e. all the additive noise from back end electronics is negligible and if there are no non-thermal noise inputs from the source) then  $\tilde{\beta}$  is equivalent to the receiver bandwidth, i.e.

$$\tilde{\beta} \equiv \beta = 4 \left( \frac{T_{\text{sky}} + T_{\text{noise}}}{\delta T_{\text{rms}}} \right)^2. \quad (\text{C.4})$$

Conversely, if the receiver output is compressed, from Eq. (2) we have that:

$$\delta V_{\text{rms}} = \frac{\partial V_{\text{out}}}{\partial T_{\text{in}}} \delta T_{\text{rms}}. \quad (\text{C.5})$$

By combining Eqs. (2), (C.3) and (C.5) we find:

$$\begin{aligned} \tilde{\beta} &= 4 \left( \frac{T_{\text{sky}} + T_{\text{noise}}}{\delta T_{\text{rms}}} \right)^2 [1 + b G_0 (T_{\text{sky}} + T_{\text{noise}})]^2 \equiv \\ &\equiv \beta [1 + b G_0 (T_{\text{sky}} + T_{\text{noise}})]^2, \end{aligned} \quad (\text{C.6})$$

which shows that  $\tilde{\beta}$  is an overestimate of the ‘‘optical’’ bandwidth unless the non linearity parameter  $b$  is very small.

## Appendix D: White noise sensitivity calibration and extrapolation to flight conditions

In this appendix we detail the calculation needed to convert the uncalibrated white noise sensitivity measured on the ground to the expected calibrated sensitivity in flight conditions. The calculation starts from the general radiometric output model in Eq. (2), which can be written in the following form:

$$T_{\text{out}}(V_{\text{in}}) = T_{\text{noise}} - \frac{V_{\text{in}}}{G_0(b V_{\text{in}} - 1)} \quad (\text{D.1})$$

Our starting point is the the raw datum, that is a couple of uncalibrated white noise levels for the two detectors in a radiometer measured with the sky load at a temperature  $T_{\text{sky-load}}$  and the front end unit at physical temperature  $T_{\text{test}}$ .

From the measured uncalibrated white noise level in  $\text{Volts}^{1/2}$ , we want to derive a calibrated white noise level extrapolated to input temperature equal to  $T_{\text{sky}}$  and with the front end unit at a temperature of  $T_{\text{nom}}$ . This is done in three steps:

1. extrapolation to nominal front-end unit temperature;
2. extrapolation to nominal input sky temperature;
3. calibration in units of  $\text{K s}^{1/2}$ .

In the following sections we will describe in detail the calculations underlying each step.

### D.1. Step 1—extrapolate uncalibrated noise to nominal front end unit temperature

This is a non-trivial step to be performed if we want to consider all the elements in the extrapolation. Here we focus on a zero-order approximation based on the following assumptions:

1. the radiometer noise temperature is dominated by the front-end noise temperature, such that  $T_{\text{noise}} \sim T_{\text{noise}}^{\text{FE}}$ ;
2. we neglect any effect on the noise temperature given by resistive losses of the front-end passive components;
3. we assume the variation of  $T_{\text{noise}}^{\text{FE}}$  to be linear in  $T_{\text{phys}}$ .

Under these assumptions the receiver noise temperature at nominal front-end temperature can be written as

$$T_{\text{noise}}(T_{\text{nom}}) = T_{\text{noise}}(T_{\text{test}}) + \frac{\partial T_{\text{noise}}^{\text{FE}}}{\partial T_{\text{phys}}} \Delta T_{\text{phys}}, \quad (\text{D.2})$$

where  $\Delta T_{\text{phys}} = T_{\text{nom}} - T_{\text{test}}$ . A similar but slightly different relationship yields for the gain factor  $G_0$ . In fact let us consider that  $G_0 = \text{const} \times G^{\text{FE}} G^{\text{BE}}$ , and that we can write  $G^{\text{FE}}(T_{\text{nom}}) = G^{\text{FE}}(T_{\text{test}})(1 + \delta)$ , where  $\delta = \frac{1}{G^{\text{FE}}(T_{\text{test}})} \frac{\partial G^{\text{FE}}}{\partial T_{\text{phys}}} \Delta T_{\text{phys}} = \frac{\ln(10)}{10} \frac{\partial G^{\text{FE}}(\text{dB})}{\partial T_{\text{phys}}} \Delta T_{\text{phys}}$ , i.e.,

$$G_0(T_{\text{nom}}) = G_0(T_{\text{test}})(1 + \delta). \quad (\text{D.3})$$

From the radiometer equation we have that  $\sigma \propto (T_{\text{in}} + T_{\text{noise}})$ , from which we can write

$$\begin{aligned} \sigma(T_{\text{nom}}) \equiv \sigma^{\text{nom}} &= \sigma(T_{\text{test}}) \frac{(T_{\text{in}} + T_{\text{noise}}(T_{\text{nominal}}))}{(T_{\text{in}} + T_{\text{noise}}(T_{\text{test}}))} = \\ &= \sigma(T_{\text{test}})(1 + \eta), \end{aligned} \quad (\text{D.4})$$

where

$$\eta = \frac{\partial T_{\text{noise}}^{\text{FE}}}{\partial T_{\text{phys}}} [(T_{\text{in}} + T_{\text{noise}}(T_{\text{test}}))]^{-1} \Delta T_{\text{phys}}. \quad (\text{D.5})$$

### D.2. Step 2—extrapolate uncalibrated noise to $T_{\text{sky}}$

From this point we will consider quantities ( $T_{\text{noise}}$ , white noise level, and  $G_0$ ) already extrapolated to the nominal front end temperature using Eqs. (D.2), (D.3) and (D.4). Therefore we will now omit the superscript ‘‘nom’’ so that, for example,  $\sigma \equiv \sigma^{\text{nom}}$ .

Let us start from the radiometer equation in which, for each detector, the white noise spectral density is given by

$$\delta T_{\text{rms}} = 2 \frac{T_{\text{in}} + T_{\text{noise}}}{\sqrt{\beta}}. \quad (\text{D.6})$$

Now we want to find a similar relationship for the uncalibrated white noise spectral density linking  $\delta V_{\text{rms}}$  to  $V_{\text{out}}$ . We start from Eq. (C.5) and calculate the derivative of  $V_{\text{out}}$  using Eq. (2) and  $\delta T_{\text{rms}}$  from Eq. (D.6). We obtain

$$\sigma = \frac{V_{\text{out}}}{\sqrt{\beta}} [1 + b G_0 (T_{\text{in}} + T_n)]^{-1}, \quad (\text{D.7})$$

where  $\beta$  is the bandwidth and  $V_{\text{out}}$  is the DC voltage output of the receiver. Considering the two input temperatures  $T_{\text{in}}$  and  $T_{\text{sky}}$ , then the ratio is

$$\frac{\sigma(T_{\text{sky}})}{\sigma(T_{\text{in}})} = \frac{V_{\text{out}}(T_{\text{sky}})}{V_{\text{out}}(T_{\text{in}})} \times \frac{1 + b G_0 (T_{\text{in}} + T_{\text{noise}})}{1 + b G_0 (T_{\text{sky}} + T_{\text{noise}})}. \quad (\text{D.8})$$

If we call  $\rho$  the ratio  $\frac{\sigma(T_{\text{sky}})}{\sigma(T_{\text{in}})}$  and use Eq. (2) to put in explicit form the ratio of output voltages in Eq. (D.8) so that  $\sigma(T_{\text{sky}}) = \rho \times \sigma(T_{\text{in}})$ , we have

$$\rho = \frac{T_{\text{sky}} + T_{\text{noise}}}{T_{\text{in}} + T_{\text{noise}}} \times \left[ \frac{1 + b G_0 (T_{\text{in}} + T_{\text{noise}})}{1 + b G_0 (T_{\text{sky}} + T_{\text{noise}})} \right]^2. \quad (\text{D.9})$$

### D.3. Step 4—calibrate extrapolated noise

From Eqs. (D.7) and (2) we obtain

$$\sigma = \frac{G_0}{[1 + b G_0 (T_{\text{sky}} + T_{\text{noise}})]^2} \times 2 \frac{T_{\text{sky}} + T_{\text{noise}}}{\sqrt{\beta}}. \quad (\text{D.10})$$

If we call  $\sigma^{\text{cal}}$  the calibrated noise extrapolated at the sky temperature and consider that, by definition,  $\sigma^{\text{cal}} = 2 \frac{T_{\text{sky}} + T_{\text{noise}}}{\sqrt{\beta}}$ , the previous equation gives

$$\sigma^{\text{cal}} = \frac{[1 + b G_0 (T_{\text{sky}} + T_{\text{noise}})]^2}{G_0} \sigma. \quad (\text{D.11})$$

## Appendix E: Weighted noise averaging

According to the LFI receiver design the output from each radiometer results from the combination of signals coming from two corresponding detector diodes. Consider two differenced and calibrated datastreams coming from two detectors of a radiometer leg,  $d_1(t)$  and  $d_2(t)$ . The simplest way to combine the two outputs is to take a straight average, i.e.,

$$d(t) = \frac{d_1(t) + d_2(t)}{2}, \quad (\text{E.1})$$

so that the white noise level of the differenced datastream is given by  $\sigma_{d(t)} = \sqrt{\sigma_{d_1(t)}^2 + \sigma_{d_2(t)}^2}$ .

This approach, however, is not optimal in cases where the two noise levels are unbalanced, so that the noise of the averaged datastream is dominated by the noisier channel.

An alternative to Eq. (E.1) is given by a weighting average in which weights are represented by the inverse of the noise levels of the two diode datastreams, i.e.,

$$d(t) = \frac{w_1 d_1(t) + w_2 d_2(t)}{w_1 + w_2}, \quad (\text{E.2})$$

or, more generally, in the case where we want to average more than two datastreams together,

$$d(t) = \frac{\sum_{j=1}^N w_j d_j(t)}{\sum_{j=1}^N w_j}. \quad (\text{E.3})$$

For noise-weighted averaging, we choose the weights as  $w_j = \sigma_{d_j(t)}^{-2}$  so that the white noise of the differenced datastream is given by:

$$\sigma_{d(t)} = \left( \sum_{j=1}^N \sigma_{d_j(t)}^{-2} \right)^{-1/2}. \quad (\text{E.4})$$

## Appendix F: Thermal susceptibility scientific requirement

Temperature fluctuations in the LFI focal plane arise primarily from variations in the sorption cooler system driven by the cycles of the six cooler compressors that “pump”<sup>7</sup> the hydrogen in the high pressure piping line to the cooler cold-end. These fluctuations show a frequency spectrum dominated by a period of  $\sim 1$  hour, corresponding to the global warm-up/cool-down cycle of the six compressors.

An active PID temperature stabilisation assembly at the interface between the cooler cold-end and the focal plane achieves stabilities of the order of 80–100 mK peak-to-peak with a frequency spectrum dominated by the single compressor frequency ( $\sim 1$  mHz) and the frequency of the whole assembly ( $\sim 0.2$  mHz).

These fluctuations propagate through the focal plane mechanical structure, so that the actual temperature instabilities at the level of the feed-amplifier systems (the term  $\Delta T_{\text{phys}}$  in Eq. (6)) are significantly damped. The LFI thermal model (Tomasi et al. 2009) shows that the fluctuations at the front-end modules are at the level of  $\lesssim 10$  mK and dominated by the “slowest” components (i.e., those with frequencies  $\lesssim 10^{-2}$  Hz).

If we take into account that slow fluctuations in the antenna temperature time stream are further damped by a factor  $\sim 10^3$  by the scanning strategy and map-making (Mennella et al. 2002), we can easily see from Eq. (6) that a receiver susceptibility  $f_{\text{trans}} \lesssim 0.1$  is required to maintain the final peak-to-peak error per pixel  $\lesssim 1 \mu\text{K}$ .

## Appendix G: Front-end temperature susceptibility parameters

Temperature susceptibility parameters are summarised in Table G.1.

## References

- Bersanelli, M., Cappellini, B., Cavaliere, F., et al. 2009, A&A, Accepted  
 Bhandari, P., Prina, M., Bowman, R. C., et al. 2004, Cryogenics, 44, 395  
 Cuttaia, F., D’Arcangelo, O., Stringhetti, L., et al. 2009, JINST, 4, T12013

<sup>7</sup> The sorption cooler does not use mechanical compressors to generate a high pressure flow, but a process of absorption-desorption of hydrogen into six hydride beds, the “compressors” controlled by a temperature modulation of the beds themselves.



**Table G.1.** Gain and noise temperature susceptibilities to front-end temperature fluctuations measured during the RCA calibration campaign.

	$\partial G/\partial T_{\text{phys}}$ (dB/K)			
	M-00	M-01	S-10	S-11
LFI18	-0.05	-0.05	-0.05	-0.05
LFI19	-0.05	-0.04	-0.02	-0.03
LFI20	-0.05	-0.04	-0.03	-0.04
LFI21	-0.07	-0.07	-0.07	-0.20
LFI22	-0.21	-0.15	-0.18	-0.13
LFI23	-0.03	-0.05	-0.05	-0.05
LFI24	-0.08	-0.06	-0.08	-0.08
LFI25	-0.02	-0.02	-0.04	-0.05
LFI26	-0.01	-0.03	-0.01	-0.01
LFI27	-0.06	-0.05	-0.04	-0.01
LFI28	-0.03	-0.07	-0.14	-0.13

	$\partial T_{\text{noise}}/\partial T_{\text{phys}}$ (K/K)			
	M-00	M-01	S-10	S-11
LFI18	0.47	0.49	0.38	0.42
LFI19	0.36	0.33	0.40	0.37
LFI20	0.25	0.23	0.30	0.25
LFI21	0.15	0.15	0.18	0.30
LFI22	0.10	0.10	0.10	0.10
LFI23	0.10	0.16	0.17	0.16
LFI24	0.40	0.41	0.10	0.43
LFI25	0.12	0.10	0.25	0.08
LFI26	0.70	0.70	0.47	0.50
LFI27	0.81	0.45	0.58	0.34
LFI28	0.15	0.15	0.10	0.33

Davis, R., Wilkinson, A., Davies, R., et al. 2009, JINST, 4, T12002  
Daywitt, W. 1989, Radiometer equation and analysis of systematic errors for the NIST automated radiometers, Tech. Rep. NIST/TN-1327, NIST  
Dupac, X. & Tauber, J. 2005, A&A, 430, 363  
Mandolesi, N., Aja, B., Artal, E., et al. 2009, A&A, Accepted  
Maris, M., Maino, D., Burigana, C., et al. 2003, Accepted for publication in A&A, astro-ph/0304089  
Martin, P., Riti, J.-B., & de Chambure, D. 2004, in ESA Special Publication, Vol. 554, 5th International Conference on Space Optics, ed. B. Warmbein, 323–331  
Meinhold, P., Leonardi, R., Artal, E., et al. 2009, JINST, 4, T12009  
Mennella, A., Bersanelli, M., Burigana, C., et al. 2002, A&A, 384, 736  
Mennella, A., Bersanelli, M., Seiffert, M., et al. 2003, A&A, 410, 1089  
Mennella, A., Villa, F., Terenzi, L., et al. 2009, JINST, 4, T12011  
Seiffert, M., Mennella, A., Burigana, C., et al. 2002, A&A, 391, 1185  
Tauber, J. 2009, A&A, Submitted  
Terenzi, L., Bersanelli, M., Battaglia, P., et al. 2009a, JINST, Submitted  
Terenzi, L., Lapolla, M., Laaninen, M., et al. 2009b, JINST, 4, T12015  
Terenzi, L., Salmon, M., Colin, A., et al. 2009c, JINST, 4, T12012  
Tomasi, M., Cappellini, B., Gregorio, A., et al. 2009, JINST, Submitted  
Valenziano, L., De Rosa, A., Cuttaia, F., et al. 2009, JINST, 4, T12005  
Varis, J., Hughes, N., Laaninen, M., et al. 2009, JINST, 4, T12001  
Villa, F., Bersanelli, M., Burigana, C., et al. 2002, in American Institute of Physics Conference Series, Vol. 616, Experimental Cosmology at Millimetre Wavelengths, ed. M. de Petris & M. Gervasi, 224–228  
Villa, F., Bersanelli, M., Cappellini, B., et al. 2009, A&A, Submitted

Wade, L., Bhandari, P., Bowman, J. R., et al. 2000, in Advances in Cryogenic Engineering, ed. et al. Kluwer Academic/Plenum New York Q-S. Shu, Vol. 45A, 499–506  
Zonca, A., Franceschet, C., Battaglia, P., Villa, F., & Mennella, A. 2009, JINST, 4, T12010

- <sup>1</sup> Università degli Studi di Milano, Dipartimento di Fisica, Via Celoria 16, 20133 Milano, Italy
- <sup>2</sup> INAF-IASF – Sezione di Bologna, Via Gobetti 101, 40129 Bologna, Italy
- <sup>3</sup> CNR – Istituto di Fisica del Plasma, Via Cozzi 53, 20125 Milano, Italy
- <sup>4</sup> Jodrell Bank Centre for Astrophysics, School of Physics & Astronomy, University of Manchester, Manchester, M13 9PL, U.K.
- <sup>5</sup> INAF – Osservatorio Astronomico di Trieste, Via Tiepolo 11, 34143 Trieste, Italy
- <sup>6</sup> Università degli Studi di Trieste, Dipartimento di Fisica, Via Valerio 2, 34127 Trieste, Italy
- <sup>7</sup> Jet Propulsion Laboratory, California Institute of Technology, 4800 Oak Grove Drive, Pasadena, CA 91109, USA
- <sup>8</sup> University of California at Santa Barbara, Physics Department, Santa Barbara CA 93106-9530, USA
- <sup>9</sup> Planck Science Office, European Space Agency, ESAC, P.O. box 78, 28691 Villanueva de la Caada, Madrid, Spain
- <sup>10</sup> INAF-IASF – Sezione di Milano, Via Bassini 15, 20133 Milano, Italy
- <sup>11</sup> Thales Alenia Space Italia, S.S Padana Superiore 290, 20090 Vimodrone (Milano), Italy
- <sup>12</sup> Departamento de Ingeniera de Comunicaciones, Universidad de Cantabria, Avenida De Los Castros, 39005 Santander, Spain
- <sup>13</sup> Instituto de Fisica De Cantabria, Consejo Superior de Investigaciones Cientificas, Universidad de Cantabria, Avenida De Los Castros, 39005 Santander, Spain
- <sup>14</sup> Agenzia Spaziale Italiana, Viale Liegi 26, 00198 Roma, Italy
- <sup>15</sup> Instituto de Astrofisica de Canarias, Vía Láctea, E-38200 La Laguna (Tenerife), Spain
- <sup>16</sup> DA-Design Oy, Keskuskatu 29, 31600 Jokioinen, Finland
- <sup>17</sup> Ylinen Electronics Oy, Teollisuustie 9 A, 02700 Kauniainen, Finland
- <sup>18</sup> Institute of Theoretical Astrophysics, University of Oslo, P.O. box 1029 Blindern, N-0315 Oslo, Norway
- <sup>19</sup> Joint ALMA Observatory, Las Condes, Santiago, Chile
- <sup>20</sup> Research and Scientific Support Dpt, European Space Agency, ESTEC, Noordwijk, The Netherlands
- <sup>21</sup> National Radio Astronomy Observatory, 520 Edgemont Road, Charlottesville VA 22903-2475, USA
- <sup>22</sup> University of Helsinki, Department of Physics, P.O.Box 64 (Gustaf Hllstrmin katu 2a) FI-00014 University of Helsinki, Finland
- <sup>23</sup> Helsinki Institute of Physics, P.O.Box 64 (Gustaf Hllstrmin katu 2a) FI-00014 University of Helsinki, Finland
- <sup>24</sup> Metsähovi Radio Observatory, Helsinki University of Technology, Metshovintie 114 FIN-02540 Kylmäla, Finland
- <sup>25</sup> MilliLab, VTT Technical Research Centre of Finland, Tietotie 3, Otaniemi, Espoo, Finland